ELSEVIER

Chemical Engineering Science 63 (2008) 2317–2329

Chemical Engineering Science

www.elsevier.com/locate/ces

Effect of precursor loading on non-spherical TiO_2 nanoparticle synthesis in a diffusion flame reactor

Ming-Zhou Yu[a], Jian-Zhong Lin[a,b,*], Tat-Leung Chan[c]

[a]*State Key Laboratory of Fluid Power Transmission and Control, Zhejiang University, Hangzhou 310027, PR China*
[b]*China Jiliang University, Hangzhou 310018, PR China*
[c]*Department of Mechanical Engineering, The Hong Kong Polytechnic University, Hung Hom, Kowloon, Hong Kong*

Received 2 November 2006; received in revised form 15 October 2007; accepted 5 November 2007
Available online 13 November 2007

Abstract

A numerical method of combining computational fluid dynamics with the particle kinetics theory is developed to study the effect of precursor loading on non-spherical TiO_2 nanoparticle synthesis in a diffusion flame reactor. A one-step chemical kinetics approach is employed to model precursor $TiCl_4$ oxidation that leads to particle formation. An efficient quadrature method of moments (QMOM) and the combustion model based on the eddy dissipation concept (EDC) together with k–ε turbulence model are used to approximate the particle kinetics evolution and the flame fields, respectively. Excellent agreements between the predicted and experimental data, with respect to the flame temperature distribution and particle kinetics, are obtained. For the final product of nanoparticles in the same flame field, the results show that the increasing of precursor loading leads to the larger agglomerated particles with larger size distribution. The primary particle number and size per agglomerate also increases with increasing the precursor loading, while the total specific surface area (SSA) decreases. The variation of inlet precursor loading has a negligible effect on the particle surface fractal dimension if only the variable of precursor loading is considered. As the inlet precursor loading is fixed, the increasing of carrying gas rate leads to the smaller agglomerated particles with increasing of total SSA and width of particle size distribution.

Keywords: TiO_2 nanoparticle synthesis; Inlet precursor loading; Coagulation; Sintering; Numerical simulation

1. Introduction

Nowadays, many synthesis of TiO_2 nanoparticles mainly occur in a diffusion flame reactor by gas-to-particle conversion. For many commercial applications, the quality of product particles depends strongly on the particle size and morphology. Although the desired particles can be generated through the controlling temperature and precursor concentration (Akhtar et al., 1991), the fundamental physics of non-spherical particle evolution in a flame reactor is still limited. This is because the complex interplay between diffusive mixing (i.e., fluid-dynamic, thermal and chemical processes) and particle growth in synthesis is difficult to be observed experimentally (Wang and Garrick, 2005). To improve the characteristics of product nanoparticles, there is a need for developing an efficient mathematical model by combining the flame dynamics with particle kinetics theory to accurately simulate the formation and growth of particles.

In general, the particles in the flame reactors are generated by chemical reactions and then are coagulated to form chain-like aggregates. As these aggregates experience a high temperature in the downstream, their figures are usually turned into nearly spherical shape (Wang and Garrick, 2005). Pratsinis and Vemury (1996) indicated that the characteristics of product nanoparticles arise mainly from the competition between the coagulation and coalescence. In principle, the variance of precursor concentration leads to the change of particle coagulation and coalescence rate as well as the particle residence time, which affects the characteristics of nanoparticles (i.e., particle size, shape and specific surface area (SSA)).

* Corresponding author. State Key Laboratory of Fluid Power Transmission and Control, Zhejiang University, Hangzhou 310027, PR China. Tel.: +86 571 86836009; fax: +86 571 87951464.
E-mail address: mecjzlin@public.zju.edu.cn (J.-Z. Lin).

0009-2509/$ - see front matter © 2007 Published by Elsevier Ltd.
doi:10.1016/j.ces.2007.11.008

Formenti et al. (1972) made an early study for the effect of precursor concentration on the characteristics of product nanoparticles through investigating TiO_2 particles in an oxygen–hydrogen diffusion flame reactor. They found that the precursor concentration is a key factor affecting the particle morphology. In the synthesis of GeO_2 nanoparticles, Pratsinis and Vemury (1996) observed that the precursor concentration significantly affects the sequence of particle formation and growth. Pratsinis et al. (1996) further investigated the role of precursor concentration in the diffusion flame reactors. They indicated that the increasing of precursor concentration results in larger primary particle size but smaller SSA of the produced TiO_2 particles. Similar results were also obtained in synthesis of SiO_2 particles in the premixed flames (Ulrich, 1971; Ulrich and Riehl, 1982). In addition, a special experimental study for the effect of precursor in a diffusion synthesis of SiO_2 nanoparticles was performed (Briesen et al., 1998). The results showed that the effect of precursor concentration on the characteristics of produced particles in a diffusion flame reactor is consistent with the experiments in a premixed flame reactor. Recently, Wang and Garrick (2005) have used a direct numerical simulation (DNS) method to simulate the TiO_2 synthesis in a two-dimensional methane–air flame, by which the spatial-temporal evolution of the fluid, chemical and particle fields were obtained. The numerical results indicated that the mean particle diameter and geometric standard deviation increase with the increasing initial precursor concentration.

Although extensive studies about the role of precursor concentration on the particle characteristics had been performed, most of these investigations focused on the particle kinetics in terms of particle size distribution. For nanoparticle synthesis in a diffusion flame reactor, there is a need to accurately capture the detailed information of particle morphology, which usually dominates the product quality as well as its particle size distribution. However, the systematic research on this problem almost stays in a stagnation state because of the experimental difficulties encountered. Typically, the particle general dynamic equation (PGDE) is used to describe the physical process of ultrafine particles. Here, it is necessary to incorporate the PGDE equation and the chemical dynamics into the computational fluid dynamics to investigate nanoparticle evolution because the nanoparticle synthesis in the flame is a complicated physicochemical process.

Considering the surface area and size of particles to be independent variables, the analysis for non-spherical particle growth can be solved using a two-dimensional aerosol dynamics (Xiong and Pratsinis, 1993; Schwade and Roth, 2003). However, the non-linear integrodifferential PGDE equation, which accounts for the particle size distribution (PSD), is difficult to be solved directly (Upadhyay and Ezekoye, 2003). In order to break through this limitation, three promising methods have been developed, namely the moment method (MM) (Hulburt and Katz, 1964; Pratsinis, 1988; Yu et al., 2006, 2007; Chan et al., 2006; Lin et al., 2007), the sectional method (SM) (Gelbard and Seinfeld, 1980; Talukdar and Swihart, 2004) and the stochastic particle method (SPM) (Wells and Kraft, 2005; Morgan et al., 2006). Due to the relative simplicity of implementation and low computational cost, the MM has been used extensively to solve most of these aerosol problems, and has been extended successfully to approximate the nanoparticle synthesis (Li et al., 2004). The quadrature method of moments (QMOM) is a kind of improved form of the MM and has been proved to be applicable to any form of the growth laws and coagulation kernels (Upadhyay and Ezekoye, 2003). Since the introduction of QMOM (McGraw, 1997), it has been excessively applied to solve the particle aggregation–breakage population balance problems (Daniele et al., 2003; Wang et al., 2005), but there are much less studies for devoting to the nanoparticle synthesis, especially in a diffusion flame reactor.

In the present study, $TiCl_4$ as a precursor is used and the growth kinetics of TiO_2 nanoparticles in a flame reactor is studied. A one-step chemical kinetics approach is used to model $TiCl_4$ oxidation that leads to the homogeneous nucleation and particle formation. The combustion model based on the eddy dissipation concept (EDC) (Magnussen, 1981) together with a k–ε turbulence model is employed to simulate the gas temperature and velocity profiles. The efficient QMOM is used to solve the distribution of particle size and surface area by using the equation of total surface area. The mathematical model for the particle dynamics includes the kinetics of precursor reaction, nucleation, surface growth, coagulation, coalescence and thermophoresis. In order to demonstrate the validity and utility of the developed model and numerical code in the present study, a comparison between the numerical and experimental results is made. The aim of the present study is to have a better understanding of the effect of precursor concentration on the non-spherical nanoparticle formation and growth.

2. Theory

2.1. Chemical kinetics

The oxidation of $TiCl_4$ occurs in the homogeneous gas phase or at the surface of existing TiO_2 nanoparticles. In the present study, the precursor $TiCl_4$ is considered to be in a very dilute state and thus the effect of nanoparticles on the flame flow can be neglected. The transport equation of species is (McGraw, 1997):

$$\frac{\partial Y_i}{\partial t} + \frac{\partial u_j Y_i}{\partial x_j} = \frac{\partial}{\partial x_j}\left(D_i \frac{\partial Y_i}{\partial x_j}\right) + \omega_i, \tag{1}$$

where Y_i (mol/m^3) is the local concentration of species i, D_i (m^2/s) is the diffusivity of species i, ω_i (mol/m^3/s) is the rate of production by chemical reaction, and u is the velocity of the flow field. Note that $i = 1$ and 2 refer to the $TiCl_4$ and TiO_2, respectively.

In the present study, the overall reaction of $TiCl_4$ is implemented as one-step reaction (Spicer et al., 2002):

$$TiCl_{4(gas)} + O_2 \xrightarrow{k} TiO_2 + 2Cl_2, \tag{2}$$

The source term ω_i in Eq. (1) denotes the oxidation rate of $TiCl_4$ (Wang and Garrick, 2005):

$$\omega_1 = -kY_1 = -(k_g + k_s A)Y_1, \tag{3}$$

$$\omega_2 = kY_1 = (k_g + k_s A)Y_1, \tag{4}$$

where k (s^{-1}) is the overall oxidation rate of $TiCl_4$ and it is denoted by $k = k_g + k_s\ A$, k_g (s^{-1}) is the constant of gas phase reaction rate, k_s (m/s) is the constant of surface reaction rate, and A (m^{-1}) is the total surface area concentration of particles. k and k_s can be implemented as (Spicer et al., 2002):

$$k = 8.26 \times 10^4 \exp(-10\,681.0/T), \tag{5}$$

$$k_s = 49 \exp(-8933/T), \tag{6}$$

where T(K) is the gas temperature.

2.2. Particle kinetics

2.2.1. The QMOM

In order to simultaneously describe the coagulation and coalescence during the particle synthesis in flames, especially in the early stages of particle formation, the agglomerate should be characterized by not only its size, but also its surface area (Koch and Friedlander, 1990). Taking into account of the physical terms of fluid convection, thermophoretic drift, Brownian diffusion, Brownian coagulation, surface growth and nucleation, the PGDE equation of the continuous particle size distribution $N(v_p)$ based on the theory of Smagorinsky (1963) is:

$$\begin{aligned}\frac{\partial N}{\partial t} + \frac{\partial (u_j N)}{\partial x_j} + \frac{\partial ((u_{\text{th}})_j N)}{\partial x_j} \\ = \frac{\partial}{\partial x_j}\left(\Gamma \frac{\partial N}{\partial x_j}\right) + \frac{1}{2}\int_{v^*}^{v} \beta(v-v', v')N(v-v', t)N(v', t)\,\mathrm{d}v' \\ - N(v,t)\int_{v^*}^{\infty} \beta(v, v')N(v', t)\,\mathrm{d}v' \\ + \frac{\partial GN}{\partial v} + J(v^*)\delta(v - v^*),\end{aligned} \tag{7}$$

where N is the distribution function of particle size based on the particle volume, v and v' are the particle volume, v^* is the volume of a TiO_2 monomer ($v^* \approx 3.32 \times 10^{-29} m^{-3}$) (Spicer, 2002), G is the growth rate of nucleus volume, $\beta(v, v')$ is the coagulation kernel between aerosols of two volumes, J is the nucleation rate, δ is the Kronecker Delta function and u_{th} is the thermophoretic velocity.

The nanoparticles experience a force in the direction of decreasing temperature gradient. For a small particle is investigated in this present study, the diameter of particles is usually smaller than the mean free path of gas, and thus the velocity of thermophoresis, u_{th} can be determined as (Friedlander, 2000):

$$u_{\text{th}} = \frac{-0.55\mu\nabla T}{\rho_g T}, \tag{8}$$

where ρ_g (kg/m^3) and μ (kg/m/s) are the density and viscosity of compound gas, respectively.

The particle diffusion coefficient Γ is denoted by $\Gamma = \Gamma_t + \Gamma_B$, where Γ_t is the turbulent diffusivity and Γ_B is the Brownian diffusivity. In this present study, Γ_B can be determined by Miller and Garrick (2004):

$$\Gamma_B = k_b T \frac{C_c}{3\pi\mu d_a}, \tag{9}$$

where C_c is the Cunningham correction factor, k_b is the Boltzmann constant and d_a is the mean agglomerated particle diameter.

In order to exhibit the effect of agglomerate morphology on the Brownian coagulation of particles, the collision kernel β should be dependent on the shape of the particles. In the free molecular regime, the collision kernel can be determined as (Schwade and Roth, 2003):

$$\begin{aligned}\beta(v, v') = (3/4\pi)^{1/6}(6k_b T/\rho_p)^{1/2} \\ \times (1/v + 1/v')^{1/2}[(sv)^{1/3} + (sv')^{1/3}]^2,\end{aligned} \tag{10}$$

where ρ_p is the particle density, the collision factor s is a function of the shape and size of the nanoparticles, and is used to calculate the collision kernel of the irregular shaped particles. The detailed definition for s is presented in Section 4.6.

The fourth term on the right side of Eq. (7) accounts for the gain/loss of particles from/to that size class by the surface growth of particles. In the present study, the growth of TiO_2 particles is considered as limited reaction and the surface reaction is the first order with respect to $TiCl_4$ concentration Y_1, and then the growth rate G is (Pratsinis, 1998):

$$G = k_s Y_1 A N_{\text{av}} v^* \tag{11}$$

where N_{av} is the Avogadro's number and A is the surface area concentration of TiO_2 particles.

For the term of homogeneous nucleation in Eq. (7), the nucleation rate J is equal to the production rate of TiO_2 particles because the critical nucleation size of TiO_2 particles is assumed to be the monomer size. According to the chemical kinetics model, the nucleation rate J is calculated as (Pratsinis, 1998):

$$J(v^*) = k_g Y_1 N_{\text{av}}. \tag{12}$$

The general dynamics equation in Eq. (7) fully describes the growth of particle size but it consumes a huge computational time. Hence, an efficient QMOM is used for solving the similar dynamics equations in the present study. A number of density function in terms of particle volume is considered. The moments of the PSD are defined as

$$m_k = \int_0^{\infty} N v^k\,\mathrm{d}v, \tag{13}$$

and thus the transport equation for the kth moment is (Talukdar and Swihart, 2004):

$$\frac{\partial m_k}{\partial t} + \frac{\partial (u_j + (u_{\text{th}})_j) m_k}{\partial x_j} = \frac{\partial}{\partial x_j}\left(\Gamma \frac{\partial m_k}{\partial x_j}\right) + k\int_0^\infty v^{k-1} G(v) N(v,t)\,\mathrm{d}v + J(v^*)v^{*k} + \frac{1}{2}\int_0^\infty \int_0^\infty [(v+v')^k - v^k - v'^k] \times \beta(v,v') N(v,t) N(v',t)\,\mathrm{d}v\,\mathrm{d}v' \quad (k=0,1,2,\ldots). \tag{14}$$

In order to employ the QMOM, the following assumption is used:

$$m_k = \int_0^{+\infty} N(v) v^k\,\mathrm{d}v \approx \sum_{i=1}^{\mathrm{NQ}} \omega_i v_i^k, \tag{15}$$

where NQ is the order of the quadrature formulation, v_i is the particle volume and ω_i is the number intensity. Substituting Eq. (15) into Eq. (14), the results in the closed equations based on the particle volume for m_k:

$$\frac{\partial m_k}{\partial t} + \frac{\partial (u_j + (u_{\text{th}})_j) m_k}{\partial x_j} = \frac{\partial}{\partial x_j}\left(\Gamma \frac{\partial m_k}{\partial x_j}\right) + k\sum_{i=1}^{\mathrm{NQ}} v_i^{k-1} G(v_i)\omega_i + J(v^*)v^{*k} + \frac{1}{2}\sum_{i=1}^{\mathrm{NQ}}\sum_{j=1}^{\mathrm{NQ}} [(v_i+v_j)^k - v_i^k - v_j^k]\beta(v_i,v_j)\omega_i\omega_j \quad (k=0,1,2,\ldots), \tag{16}$$

where weights (ω) and abscissas (v) are determined through the product–difference (PD) algorithm from the low-order moments (Li et al., 2004). In order to simplify the treatment and avoid the numerical diffusion, the moment m is non-dimensionalized by the characteristic moment. The kth characteristic moment m_{k0}, is implemented as

$$m_{k0} = \omega_0 \times v^{*k}, \quad (k=0,1,2,\ldots), \tag{17}$$

where ω_0 is the value of the monomer number as the feed precursor loading is chosen to be its reference and all precursors are completely oxidized.

2.2.2. Surface area model

Tracing the total surface area per unit volume of the particles is a very important issue, not only in order to gain information on the particle morphology, but also to calculate more realistic collision kernels. Taking into the consideration of convection, diffusion, nucleation and coalescence processes, the total surface area per unit volume A can be represented as (Giesen, 2004):

$$\frac{\partial A}{\partial t} + \frac{\partial u_j A}{\partial x_j} = \frac{\partial}{\partial x_j}\left(\Gamma \frac{\partial A}{\partial x_j}\right) + J(v^*)a_{p0} - \frac{1}{\tau_f}(A - A_{\min}), \tag{18}$$

where a_{p0} is the surface area of a TiO_2 monomer, τ_f is the characteristic sintering time and $A_{\min}$ is the minimal total surface area per unit volume as each agglomerate is separately reduced to a sphere. It should be noted that the total surface area per unit volume A is not affected by coagulation. In the present developed numerical codes, the minimal total surface area per unit volume is solved using the moment equations:

$$A_{\min} = (\pi m_0)^{1/3}(6m_1)^{2/3}. \tag{19}$$

The characteristic coalescence time τ_f in Eq. (18) is the key variable, and depends on many factors such as temperature, primary particle size, material and sintering mechanism. Moreover, the sintering mechanism concerns viscous flow, lattice diffusion, surface diffusion or grain boundary diffusion. Up to now, several attempts have been taken to tackle for this annoying problem (Artelt et al., 2003; Giesen et al., 2004). In the present study, the method of Johannessen et al. (2001) is used and the characteristic coalescence time τ_f is defined as:

$$\tau_f = k_0 d_p^m \frac{T}{T_0}\exp\left(\frac{E_A}{R}\left(\frac{1}{T} - \frac{1}{T_0}\right)\right), \tag{20}$$

where E_A is the activation energy, d_p is the initial diameter of the two primary contacting particles in an aggregate, k_0 is the pre-exponential term at the temperature T_0 and R is the universal gas constant. In the present study, E_A, k_0 and m used are $E_A = 1.5\times10^5$ J/mol, $k_0 = 1.0\times10^{28}\,\mathrm{m}^{-4}$ and $m = 4$, respectively.

Similar to the solution for sintering rate by Johannessen et al. (2001), the last term on the right side of Eq. (18) is denoted by a variable R_s:

$$R_s = \frac{A - A_{\min}}{\tau_f}, \tag{21}$$

thus the sintering rate for the total surface area per unit volume can be expressed as

$$R_s = \begin{cases} \dfrac{A - A_{\min}}{\tau_f(d_p^*)} & d_p^* = \left(\dfrac{6(v/2)}{\pi}\right)^{1/3} \quad \text{for } n_p < 2, \\ (n_p - 1)\left(\dfrac{0.41 a_p}{\tau_f(d_p)}\right) & \text{for } n_p > 2, \end{cases} \tag{22}$$

where d_p and a_p are diameter and surface area of the primary particles, respectively, and the primary particle number n_p in an aggregation can be directly obtained through the QMOM and surface area equations:

$$d_p = \frac{6m_1}{A}, \quad a_p = \pi\left(\frac{6m_1}{A}\right)^2, \quad n_p = \frac{1}{36\pi}\frac{A^3}{m_1^2 m_0}. \tag{23}$$

3. Simulation of configuration and numerical method

Fig. 1 shows the configuration of the simulated burner which is consistent with the experimental setup (Pratsinis et al., 1996). It allows a precise control of simulation validation. The burner is a multiple concentric-tube setup which is fed by methane, air and argon gas saturated with the $TiCl_4$ vapor at a controlled temperature. The diameter of the central tube is 4 mm and the spacing between the successive tubes is 1 mm. All tubes have a wall thickness of 1 mm. The simulated design of these seven

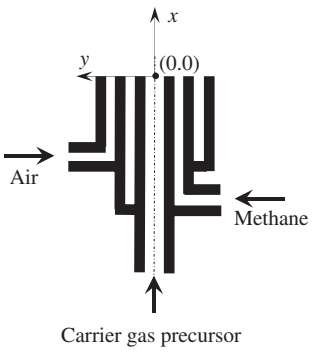

Fig. 1. The configuration of the simulated burner.

Table 1
Reactant flow rate and precursor loading for synthesis of TiO_2 nanoparticle by $TiCl_4$ oxidation

Case no.	Air (l/min)	CH_4 (l/min)	Ar (l/min)	$TiCl_4$ (mol/min)	$TiCl_4$ (mol/m^3)
1	3.8	0.226	0.25	0.4×10^{-4}	0.16
2	3.8	0.226	0.25	1.6×10^{-4}	0.64
3	3.8	0.312	0.25	1.6×10^{-4}	0.64
4	3.8	0.407	0.25	1.6×10^{-4}	0.64
5	3.8	0.226	0.25	5.8×10^{-4}	2.32
6	3.8	0.312	0.25	5.8×10^{-4}	2.32
7	3.8	0.407	0.25	5.8×10^{-4}	2.32
8	3.8	0.226	0.50	1.6×10^{-4}	0.32

investigations which comprises a constant air feed rate, three levels of methane feed rate and two levels of argon feed rate is listed in Table 1. In order to highlight the effect of the precursor loading on the particle kinetics, three levels of $TiCl_4$ feed loading used are 0.4×10^{-4}, 1.6×10^{-4} and 5.8×10^{-4} mol/ min, respectively. Table 1 summarizes the inlet precursor concentrations in terms of $TiCl_4$ feed loading and argon flow rate (i.e. 0.16, 0.32, 0.64 and 2.32 mol/m^3).

In the present study, the flow, temperature and particle fields in the flames are all incorporated into the developed numerical code in terms of consistent semi-implicit method for pressure-linked equations (SIMPLC) approach. All the governing equations are discreted by the finite-volume method. The quadratic upwind interpolation of convective kinematics (QUICK) scheme is adopted for the convective terms in Eqs. (16) and (18), momentum and energy equations. The spatial coordinates are $r = [x, y]$ where x and y are the streamwise and the cross-stream directions, respectively. A structured grid is made for the confined computational domain axially from $x = -0.005$ to $x = 0.115$ m (i.e. from 0.005 m below the burner mouth to 0.115 m above the burner mouth) and radially from $y = -0.07$ to $y = 0.07$ m. The number of computational grid is distributed by $x_{grid} \times y_{grid}$ (i.e. 6000 × 1000 grids). The temperature of burner and all gases are initialized to be 450 K in order to avoid the precursor condensation. Since some recent studies (Daniele et al., 2003; Marchisio et al., 2003a, b) have shown that a quadrature approximation with three nodes (NQ = 3) is sufficient to describe the moment evolution with a good accuracy, the order of the quadrature formula in Eq. (15) used is 3 in all present simulations. The calculation of turbulent flow field in the flame is based on the solution of the Reynolds-averaged Navier–Stokes (RANS) equations in the compressible formulation together with the k–ε turbulence model. The transport equations for the mass, the velocity vector u_i (m/s), the turbulent kinetic energy k (m^2/s^2), the dissipation rate of turbulent kinetic energy ε (m^2/s^3) and the enthalpy h (J/kg) are solved simultaneously. In order to describe exactly the flame temperature distribution, the eddy-dissipation-concept (EDC) based combustion model (Magnussen, 1981) is carried out. This model is based on a general flame reactor concept for the calculation of the average net species production rates in the turbulent reactive flows, and the combustion is assumed to take place in the region of the turbulent field where the highest molecular flux occurs.

To build up the numerical model, some additional approximations and assumptions are made:

(1) The flame flow field is not affected by the existence of particles since the product particles are assumed to be in a very dilute state.
(2) $TiCl_4$ oxidation reaction has no effect on the flame temperature due to the low precursor, i.e. only the methane combustion reaction dominates the temperature fields.
(3) Only the Brownian coagulation is considered. For particle diameter smaller than 100 nm, the coagulation induced by turbulence can be neglected.
(4) Due to the fast oxidation of precursor $TiCl_4$ in the reaction zone, the supersaturation of TiO_2 atoms in the reaction zone is very high. As TiO_2 is formed, it appears in the form of 3.32×10^{-29} m^3 volume of a monomer. This leads to the assumption that the monomers (i.e. TiO_2 molecule) can be regarded as the critical clusters, which subsequently grow by both coagulation and surface growth of particles.
(5) Particle evaporation is not considered since the monomers are usually in a supersaturation state.
(6) The hydrolysis of $TiCl_4$ is not considered in the present study.

4. Results and discussion

4.1. Flame structures and validation

Fig. 2 shows the temperature distributions of calculated flame structures which corresponds to the conditions of Table 1, in order to illustrate the flame structure. From the comparison of Flame A, B and C, it can be seen that increasing of methane flow rate will increase the temperature and height of the flame, which qualitatively conforms to the visual appearance of the experimental flames given by Johannessen et al. (2000). Flames A, B and C show only a single flame front exists on the axis. The result also shows that the higher flow rate of methane leads to the larger flame region. Along the flame axis, it is earlier to approach the high temperature in flame A than in flame D. It reveals that the significant mixing between the methane and air is more easily attained as the central nozzle flow rate is low,

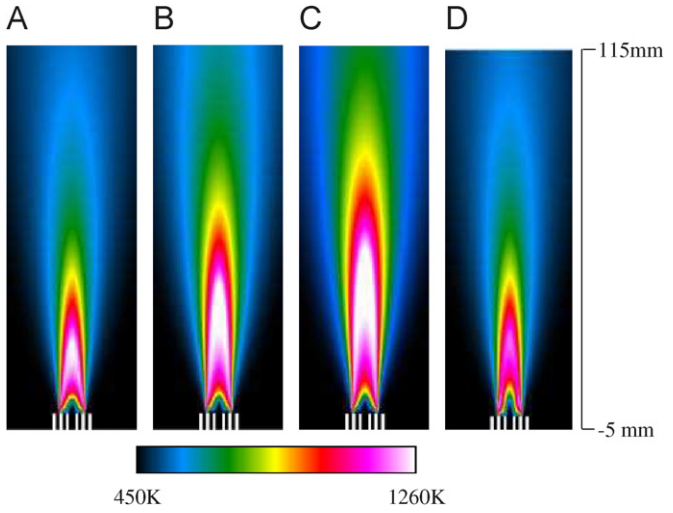

Fig. 2. Temperature contour plots of the case 2 (A), case 3 (B) and case 4 (C) in Table 1 at constant argon flow rate of 0.25 l/min, and case 8 (D) at constant argon flow rate of 0.5 l/min. Each flame has a constant air flow rate of 3.8 l/min.

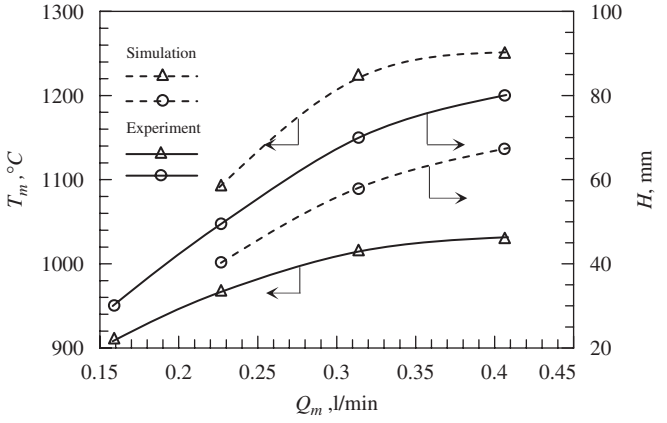

Fig. 3. Comparisons of numerical and experimental data (Pratsinis et al., 1996) for the maximum flame temperature and flame height as a function of methane flow rate.

and thus the higher flame temperature appears certainly.

The comparison between the measured and numerical data for the flame maximum temperature T_m and height H as a function of methane flow rate Q_m are shown in Fig. 3, where the experimental results obtained from Pratsinis et al. (1996) are also given. The numerical results are in good agreement with the experimental ones for both of their maximum flame temperature and flame height. It should be noted that the maximum flame temperature is assumed to be at the tip of a diffusion flame. The increasing of methane flow rate from 0.159 to 0.407 l/min leads to the increasing of measured maximum flame temperature from 909 to 1026° which is consistent with the numerical results obtained for the increasing of maximum flame temperature from 1080 to 1240° while the methane flow rate is increased from 0.226 to 0.407 l/min. The results of flame height also show a good agreement between the experiment and numerical simulation. Increasing of methane flow rate from 0.159 to 0.407 l/min will lead to an increase of the measured flame

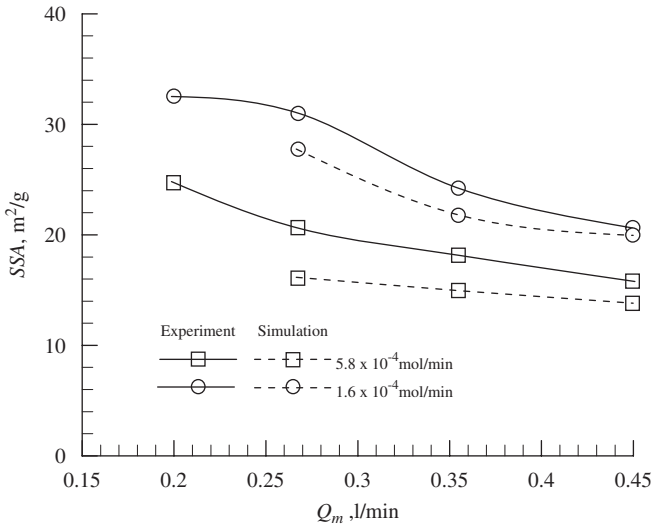

Fig. 4. Comparisons of numerical and experimental data (Pratsinis et al., 1996) for the specific surface area as a function of methane flow rate at two different $TiCl_4$ loadings. The air and argon flow rates are fixed to be 3.8 and 0.25 l/min, respectively.

height from 30 to 80 mm, while the numerical flame height will increase from 40 to 70 mm as the methane flow rate increases from 0.226 to 0.407 l/min.

In order to validate the developed numerical code used in the present study, the SSA is solved by using the combination of PGDE equations and surface area equation, and the numerical results are then compared with the experimental ones (Pratsinis et al., 1996). In the present study, the simulated total SSA of particles is defined as $A/M_1\rho_p$ for the 3-point calculation where ρ_p is the bulk solid density. For the convenience of comparison, the values of numerical SSA are averaged because the experimental data obtained from Pratsinis et al. (1996) were averaged one. Hence, the SSA of particles is calculated by $\int A/(m_1\rho_p)\,\mathrm{d}L/L$ at the outflow interface ($x = 0.115$ m) where L is the position vector as shown in Fig. 4. For the identical methane flow rate cases, the measured and numerical results show that the increasing of precursor $TiCl_4$ loading will decrease the SSA of the particles. In addition, as the precursor loading is fixed, the SSA of particles decreases with increasing of methane flow rate. When $TiCl_4$ loading is 1.6×10^{-4} mol/ min, for example, the experimental SSA of particles is decreased by 40% as the methane flow rate increases from 0.159 to 0.407 l/min. This is consistent with the numerical results in which the SSA of particles decreases 25% as the methane flow rate increases from 0.226 to 0.407 l/min. Similar conclusion is also drawn from the precursor $TiCl_4$ loading of 5.8×10^{-4} mol/ min. Furthermore, Pratsinis et al. (1996) revealed that increasing of precursor loading will result in a slow variation of SSA as the methane flow rate increases. They attributed it to the change of particle size and sintering rate.

4.2. Analysis of $TiCl_4$ reaction rate

The reaction rates of $TiCl_4$ molecules are strongly related to the flame temperature and velocity distributions. Fig. 5 shows

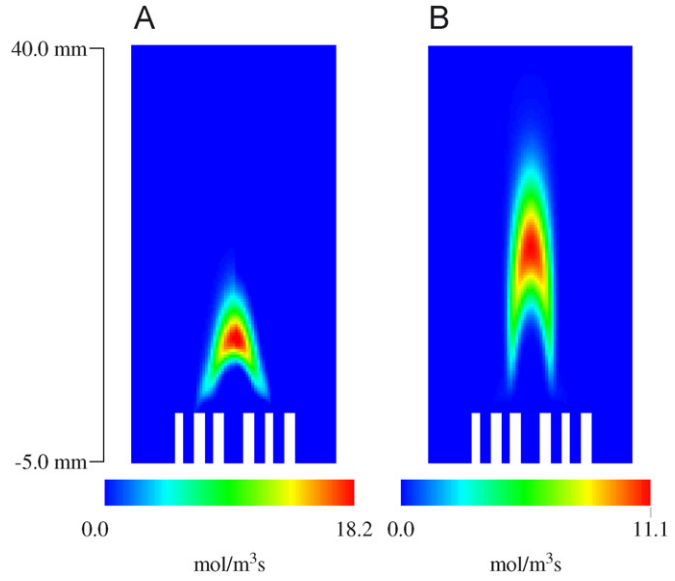

Fig. 5. The contour plots of $TiCl_4$ precursor oxidation rates as the argon flow rates are 0.25 μmin (A) and 0.5 l/min (B), respectively. The corresponded inlet precursor concentrations are 0.64 and 0.32 mol/m^3, respectively.

the contours of $TiCl_4$ precursor oxidation rates as the argon flow rates are 0.25 and 0.5 l/min, respectively, which corresponds to the cases 2 and 8 in Table 1. In Fig. 2, the higher argon flow rate, the farther distance from the burner for high temperature, which consequently makes the precursor reaction zone move downstream, as shown in Fig. 5. For the argon flow rate of 0.25 l/min, $TiCl_4$ oxidation mainly occurs from 5 to 15 mm above the burner mouth, while the reaction of $TiCl_4$ for the argon flow rate of 0.5 l/min mainly occurs from 15 to 30 mm above the burner mouth. Since the precursor reaction is the initial stage for the nanoparticle synthesis in the flame reactor, this difference of main precursor reaction distribution will certainly affect the further formation and growth of nanoparticles, especially for the evolution of particle size and shape.

4.3. Analysis of particle characteristics in terms of the particle size distribution

As the particles form from $TiCl_4$ oxidation and then coagulate to the larger aggregates, their particle number concentration initially increases and then decreases in the flame reactor. This can be revealed in the axial variation of the zero moment m_0 as shown in Fig. 6(a). In order to highlight the effect of precursor concentration on the particle kinetics, the flow rates of inlet air, methane and argon are settled to be invariable values to obtain the identical flame structures. In Fig. 6, the precursor loadings of cases 1, 2 and 5 in Table 1 are 0.4×10^{-4}, 1.6×10^{-4} and 5.8×10^{-4} mol/ min, respectively. Fig. 6(a) shows that there is an enormous increase of particle numbers above the burner mouth due to the high $TiCl_4$ oxidation rate and low coagulation rate, while the particle number is zero in the regions near the burner for all three studied cases. It is because the temperature in the regions near the burner is low enough to avoid $TiCl_4$ oxidation for taking place. As the temperature increases along the downstream, the particle collision accelerates which results in the particle number intensity drops rapidly due to the higher coagulation rate. When the flame temperature decreases further along the downstream, the particle number intensity decreases slowly due to the increasing of characteristic coagulation time. The particles are agglomerated and made up of some smaller primary particles by coagulation or sintering processes. Fig. 6(a) also reveals that the increasing of precursor $TiCl_4$ concentration will result in a larger particle number intensity throughout the flame height. In the flame zone at about $x = 0.01$ m where the monomers are mainly formed from the precursor oxidation, the difference of m_0 among these three studied cases reaches their maximum value and then decreases as the particles move along the downstream. This is attributed to the effect of coagulation variation on the particle kinetics. At higher precursor concentration, the production rate of initial particles is higher which provides more opportunities of the particles to be collided due to the higher coagulation rate. Therefore, the particle number decreases more sharply as the precursor loading is higher. Obviously, Fig. 6(a) shows the deviation of three curves reaches their minimum value at the flame reactor outlet ($x = 0.115$ m).

The effect of the precursor concentration on the particle kinetics can be further quantified by the mean volume-based particle diameter, d_a. The mean particle volume, v_p, is computed from the first two moments as $v_p = m_1/m_0$ and the mean diameter is given by $d_a = (6v_p/\pi)^{1/3}$ (Settumba and Garrick, 2003). The comparisons of d_a among the precursor loadings of 0.4×10^{-4}, 1.6×10^{-4} and 5.8×10^{-4} mol/ min are shown in Fig. 6(b). The variation of diameter is not significant in the flame regions above the burner mouth, and then there is an enormous increase in particle diameter along the downstream due to the high particle coagulation rate. In a further downstream region, the low collision rate results in a slow increase in particle diameter. As the inlet $TiCl_4$ loading is increased from 0.4×10^{-4} to 5.8×10^{-4} mol/ min, the increasing of initial particle number concentration increases the diameter of product nanoparticles ($x = 0.115$ m) from 150 to 300 nm. It indicates that the controlling of inlet precursor loading is an effective way to produce the desired nanoparticles.

Besides the particle number intensity and diameter, the SSA is another key parameter for determining the properties of nanoparticles. The SSA is also significantly affected by the precursor loading. Fig. 6(c) shows the variations of SSA along the flame axis as the precursor $TiCl_4$ loadings are 0.4×10^{-4}, 1.6×10^{-4} and 5.8×10^{-4} mol/ min, respectively. In Fig. 6(c), the increasing of precursor loading from 0.4×10^{-4} to 5.8×10^{-4} mol/ min will result in a decrease of SSA from 23 to 10 m^2/m^{3}g at the flame reactor outlet. Pratsinis et al. (1996) attributed this to the enhanced sintering rate as the inlet precursor loading increases. In general, the increase of precursor loading leads to an increase of initial particle number concentration, which results in higher coagulation rates and larger agglomerates of primary particles because of more contact points, and accordingly the coalescence or sintering rate

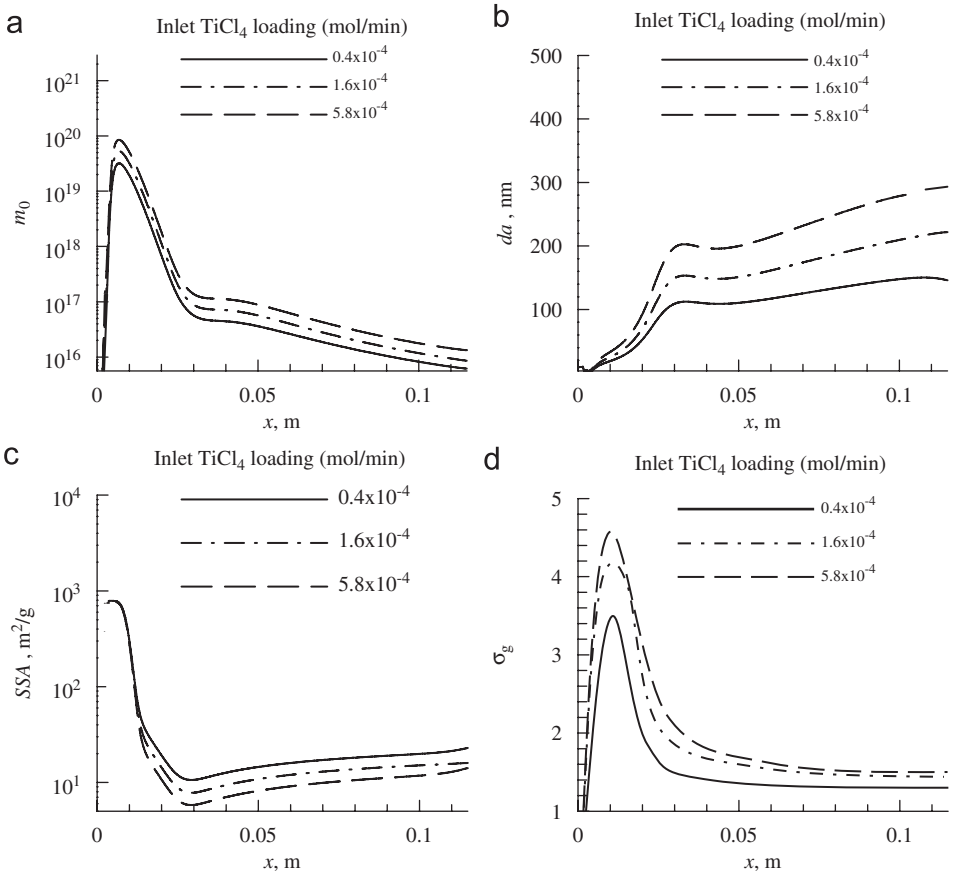

Fig. 6. The variation of particle number concentration (a), diameter (b), specific surface area (c) and geometric standard deviation (d) along the flame axis for different inlet precursor $TiCl_4$ loadings.

increases. For the three cases, a slight increase of the SSA in the regions beyond $x = 0.03$ m, i.e. beyond high temperature zone, is due to the change in density of the aerosol. In the zone within $x = 0.015$ m, three curves are nearly identical, showing that the variation of precursor loading has negligible effect on the SSA near the burner. The reason is that the temperature is low in this region, and accordingly coalescence hardly takes place. This further reveals that the variation of SSA is mainly determined by the coalescence or sintering processes, but not by coagulation.

The geometric standard deviation (GSD) is a function of the width of particle size distribution and is defined as (Pratsinis, 1988):

$$\sigma_g = e^{\hbar}, \tag{24}$$

where, $\hbar = \frac{1}{3}\ln^{1/2}(m_0 m_2/m_1^2)$. An analysis of nanoparticle synthesis suggests that the coagulating particles ultimately reach a distribution which is independent of initial conditions, i.e., the so-called self-preserving size distribution (SPSD). Hinds (2000) revealed that this particular distribution could be approached as σ_g ranges from 1.32 to 1.36, while Pratsinis (1998) took $\sigma_g = 1.46$ as a critical value denoting this distribution. The evolutions of σ_g along the flame axis at three different inlet precursor loadings are shown in Fig. 6(d). Not far from the entrance of flame reactor, the particle size distribution is almost mono-dispersed, i.e., $\sigma_g = 1$, because the particles here are mostly comprised of the primary particles with minimum size, i.e., monomers. As these particles move downstream, the coagulation gradually makes particle size distribution wider, which leads to an increase of σ_g. The reason is that the coagulation results in the formation of particles with larger size, while monomers are still being produced by precursor oxidation (Lu et al., 1999). However, as the precursor oxidation is virtually done and the coagulation predominates the particle kinetics, σ_g decreases and ultimately approaches to the SPSD at the flame reactor outlet ($x = 0.115$ m). Although Fig. 6(d) reveals that the particle size distributions can almost reach to the SPSD at the flame reactor outlet for these three cases, the values of σ_g are slightly increased as the inlet precursor loading increases. It suggests that the lower inlet precursor concentration can be used to produce the smaller particles with more uniform particle size distribution.

4.4. Analysis of characteristics of primary particles per agglomerate

In the flame region, the particles form and then immediately start to collide and synthesize the irregular agglomerates which comprise primary particles. In fact, the size and number of the primary particles per agglomerate significantly affects on the particle coagulation and sintering processes, and finally determine the properties of product nanoparticles. Therefore, it is

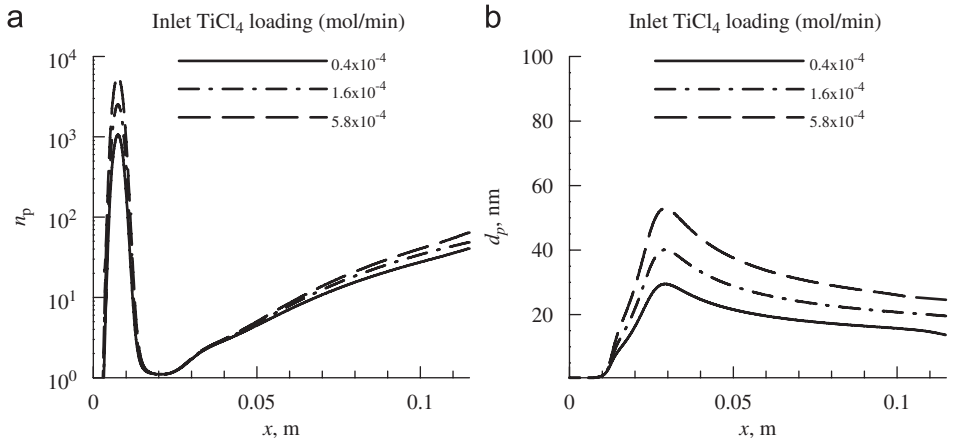

Fig. 7. The variation of primary particle number (a) and diameter (b) per agglomerate along the flame axis for different inlet precursor $TiCl_4$ loadings.

necessary to explore the kinetics of primary particles in the nanoparticle synthesis, especially the effect of precursor loading should be mainly taken into account. The distributions of primary particle diameter d_p and number n_p at two different precursor loadings along the flame axis are shown in Fig. 7. Similar to the results obtained in Fig. 6, the precursor loadings of cases 1, 2 and 5 in Table 1 are 0.4×10^{-4}, 1.6×10^{-4} and 5.8×10^{-4} mol/ min, respectively. It reveals that the increasing of precursor $TiCl_4$ loadings will result in the larger primary particle number as shown in Fig. 7(a) and the larger primary particle size as shown in Fig. 7(b) for the final product of nanoparticles. This is in agreement with the measured results given by Pratsinis et al. (1996). As the inlet $TiCl_4$ loading is increased, the initial monomer concentration also increases which results in a higher sintering rate and consequently the larger primary particle size. In the flame zone within $x = 0.012$ m as shown in Fig. 7(a), only the coagulation dominates the particle kinetics, n_p increases with increasing of inlet precursor loading. In this flame region, n_p reaches their maximum values. As these particles move along the downstream, the high temperature leads to coalescence, and then sintering dominates the particle evolution. For the three different precursor loadings, n_p decreases sharply from its maximum to around 1 at $x = 0.02$ m. At the position of $x = 0.03$ m as shown in Fig. 7(b), the primary particle diameters reach their maximum values. It shows that the sintering processes are completed and then the particle evolution is mainly dominated by the coagulation. From Figs. 7(a) and (b), the extremum positions of n_p and d_p are nearly unchanged as the inlet precursor loadings vary. Therefore, it is obvious that the particle evolution is predominated by either coagulation or coalescence process, which is mainly related to the flame temperature distribution and flame structure, but not its inlet precursor loading.

4.5. Particle morphology

As shown in Section 4.4, the agglomerates are formed essentially by the coagulation and sintering processes. If the collision rate is faster than the sintering rate, then the aggregate particles are formed. On the other hand, if the sintering rate is faster

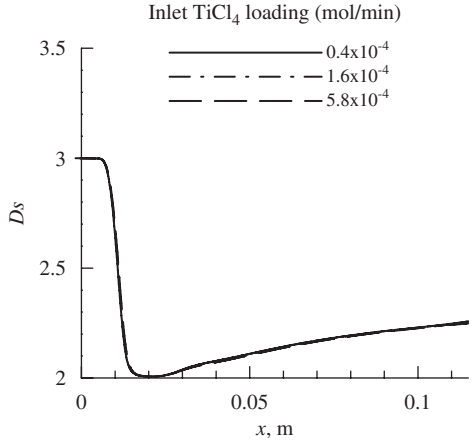

Fig. 8. The variation of surface fractal dimension along the flame axis for different inlet precursor $TiCl_4$ loadings.

than the particle collision rate, then the shaped and monolithic particles are formed regularly. The detailed definitions for the collision and sintering rates can be found in Artelt et al. (2003). In the present study, the effect of precursor loading on the particle morphology is studied, which arises primarily from the competition between the coagulation and sintering processes. The agglomerate morphology is usually approximated by an important index, the surface fractal dimension D_s which can be determined as:

$$D_s = \log_{(v_a/v^*)}(a_a/a_{p0})^3, \tag{25}$$

where v_a is the volume of an average agglomerate, v^* is the volume of a monomer, a_a is the surface area of an average agglomerate and a_{p0} is the surface area of a monomer. The variable D_s is essentially determined by the moments m_0 and m_1, and the total surface area A where $v_a = m_1/m_0$ and $a_a = A/m_0$ in this present study. In theory, the variable D_s ranges from 2 for a completely fused sphere to 3 when the primary particles just touch each other. Fig. 8 shows the variation of D_s along the flame axis at three different precursor loadings. In the flame region above the burner, many small monomers coagulate to the fractal agglomerates with D_s being close to 3 which indicates

that the sintering does not take place in this zone. As these agglomerates enter the regions along the downstream with such higher temperature, the increased sintering makes the number of primary particles as well as D_s decrease. D_s decreases to nearly 2 ranging from $x = 0.025$ to 0.035 m which implies that there is only one spherical particle per agglomerate. This result corresponds to the primary particle number approaching to 1 in the same zones as shown in Fig. 7(a). Beyond the flame region with such high temperature, the sintering stops and coagulation again makes agglomerates irregular, and thus D_s increases. Three curves overlap each other indicates that the variation of inlet precursor concentration has a negligible effect on the evolution of particle morphology. This is consistent with the above conclusion in Section 4.4 that the particle evolution is predominated by either coagulation or sintering process but not its inlet precursor loading.

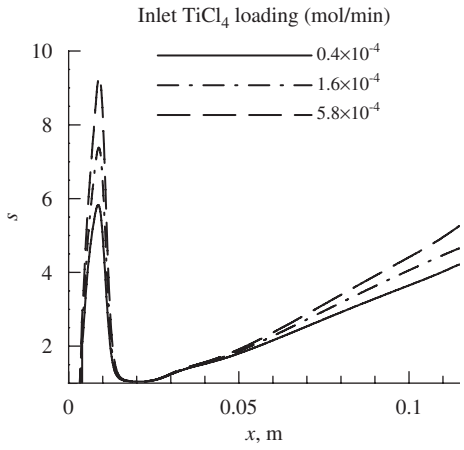

Fig. 9. The variation of particle collision factor along the flame axis for different inlet precursor $TiCl_4$ loadings.

4.6. Particle collision factor

Pratsinis (1998) pointed out that the agglomerates coagulate faster than the spherical particles in the free molecule regime because the former exhibits a larger collision area than the latter. To account for this effect, the irregular factor of particles must be employed in the computation of particle synthesis. Xiong et al. (1992) presented a collision factor s in the collision kernel and successfully applied it to simulate the nanoparticle synthesis in a wall-heated aerosol. Based on the theory of Xiong et al. (1992), the equivalent sphere volume in terms of the accessible surface area of the average agglomerate is defined by:

$$v_{\mathrm{acc}} = (36\pi)^{-1/2}(s^* a_a)^{3/2}, \tag{26}$$

where the surface accessibility s^* is the fraction of the surface area of an agglomerate. s^* is given by (Xiong et al., 1992):

$$s^* = (D_s - 2)(2v^*/v_a)^{1-\zeta} + 3 - D_s, \tag{27}$$

where ζ is the measured number of primary particles located at the surface of an agglomerate and is set to 0.8 in the present computation.

As the equivalent sphere volume v_{acc} is obtained, the collision factor s in Eq. (10) can be expressed easily as:

$$s = v_{\mathrm{acc}}/v_a. \tag{28}$$

Once the collision factor s is employed in the coagulation kernel, the simulation model is more exact to exhibit the physicochemical nature of nanoparticle synthesis in the flame reactor. Fig. 9 shows the variation of the collision factor s along the flame axis for three different precursor loadings. In theory, the large collision factor corresponds to the high coagulation rate. Fig. 9 shows that the higher precursor loading corresponds to the larger collision factor (i.e., the higher coagulation rate). It is more obvious at the flame reactor outlet and in the zone at around $x = 0.01$ m where the monomers are mainly formed. Beyond $x = 0.02$ m, the collision factor s increases as the particles move along the downstream, which is consistent with the variation of D_s in those regions as shown in Fig. 8. It reveals that the particles with irregular shapes are more easier to form into larger agglomerate.

4.7. The effect of inlet argon velocity

The precursor loading can be controlled through adjusting either the inlet precursor concentration or the flow rate of carrying gas. The inlet precursor loading of 1.6×10^{-4} mol/ min is fixed to assure an identical mass production rate. Two different inlet argon flow rates of 0.25 and 0.5 l/min are performed. The corresponding inlet precursor concentrations of cases 2 and 8 in Table 1 are 0.64 and 0.32 $\mathrm{mol/m^3}$, respectively. The immediate consequence of the variation in argon inlet velocity results from the change in the flame temperature distribution as well as the residence time of evolving the particles (Lu et al., 1999). Figs. 10(a) and (b) show the variations of aggregated particle number m_0 and diameter d_a along the flame axis for two different argon flow rates, respectively. The increased argon flow rate leads to the shortened particle residence time which allows less time for the coagulation and sintering processes of particles. These results in the smaller agglomerated particles with the higher particle number m_0. For the argon flow rates of 0.5 and 0.25 l/min, m_0 is 8×10^{16} and 1×10^{16} at the outflow region $x = 0.115$ m, respectively. Contrary to the agglomerated particle number, Fig. 10(b) shows that the particle diameter d_a is smaller for the argon flow rate of 0.5 l/min than 0.25 l/min. In the flame region near the burner mouth, the drastic variation of m_0 or d_a appears earlier in the case of argon flow rate of 0.25 l/min than 0.5 l/min, which is mainly attributed to the delay of precursor reaction as the carrying gas flow rate is increased as shown in Fig. 5. Due to the less time for the sintering of nanoparticles in a higher carrying flow rate, the SSA is less in the case of argon flow rate of 0.5 l/min than 0.25 l/min throughout the flame regions as shown in Fig. 10(c). The variation of geometric standard deviation σ_g along the flame axis is shown in Fig. 10(d). For the particles in the flame region near the outflow interface, σ_g is smaller in the case of argon flow rate of 0.25 l/min than 0.5 l/min. It indicates that the particle

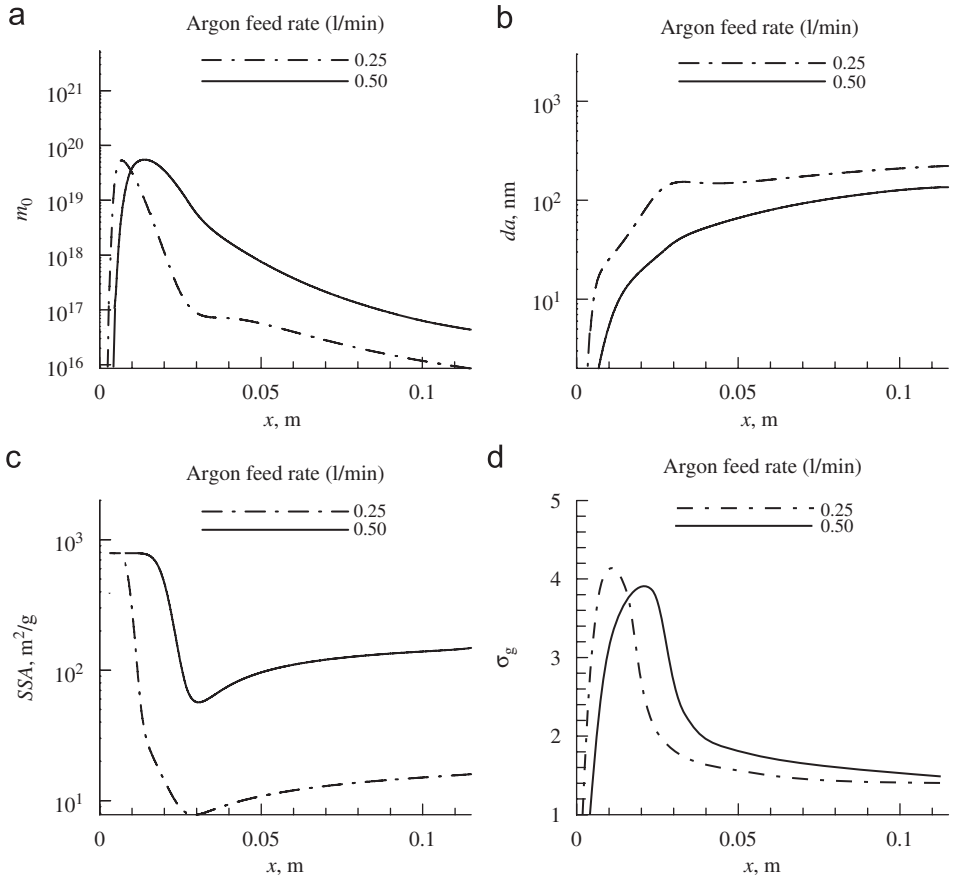

Fig. 10. The variation of particle number concentration (a), diameter (b), specific surface area (c), and geometric standard deviation (d) along the flame axis at two different argon feed rates.

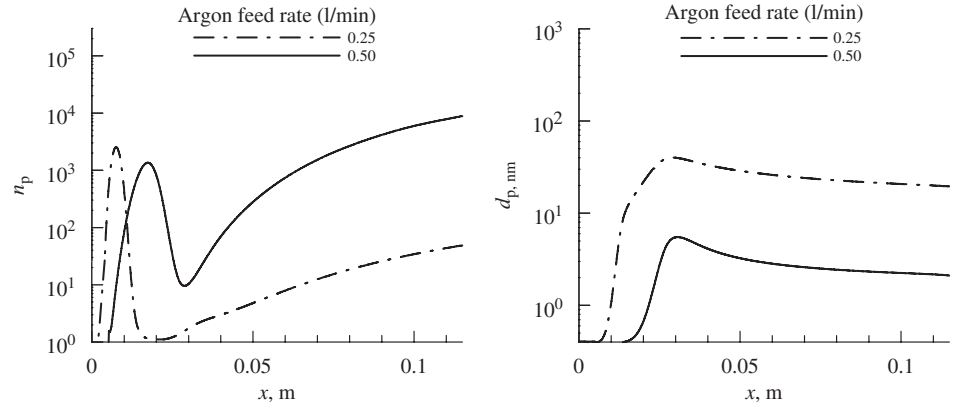

Fig. 11. The variation of primary particle number (a) and diameter (b) per agglomerate along the flame axis for two different argon feed rates.

size distribution is more nonhomogeneous as the carrying flow rate is higher.

Figs. 11(a) and (b) show the variation of the primary particle diameter d_p and number n_p per agglomerate along the flame axis for two different argon flow rates, respectively. Increasing of argon flow rate from 0.25 to 0.5 l/min will result in a decreasing of primary particle diameter and number per agglomerate from 20 to 6 nm and 10^4 to 10^2, respectively. This is attributed to the shortened particle residence time and low coagulation and sintering rates as the argon flow rate is increased. In Fig. 3, the increasing of argon flow rate will decelerate the fuel combustion. The lower flame temperatures will reduce the particle coagulation and sintering rates, and consequently lead to the formation of agglomerated particles with few primary particles is generated. In addition, the particles have less time to collide and sinter as the argon flow rate is increased due to the shortened particle residence time, which is also the main reason that the primary particle number and size are decreased. Fig. 12

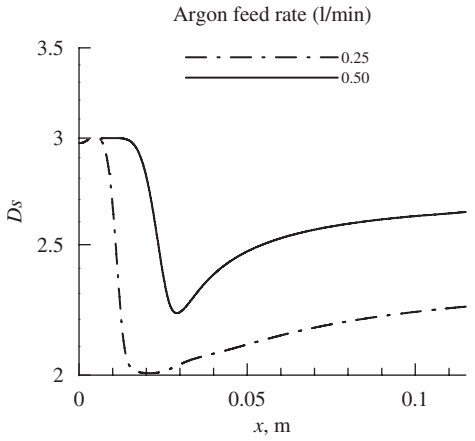

Fig. 12. The variations variation of surface fractal dimension along the flame axis for two different argon feed rates.

shows the variations of D_s along the flame axis as the argon flow rates are 0.25 and 0.5 l/min, respectively. From Section 4.5, the higher D_s corresponds to more irregular agglomerated particles. It is observed that the final particle morphology is more irregular in the case of argon flow rate of 0.25 l/min than 0.5 l/min. In the flame axial direction ranging from $x = 0.02$ to 0.04 m, the value of D_s is far from 2 for the argon flow rate of 0.5 l/min, it indicates that the separated spherical particles do not appear. It further reveals that the particles have a lower sintering rate in a diffusion flame as the argon flow rate increases.

5. Conclusions

A mathematical model embodying the particle formation and growth processes in the flame field is developed for the simulation of TiO_2 nanoparticle synthesis in a diffusion flame reactor. The effect of inlet precursor loading on the particle number, size, specific surface area (SSA) and shape is highlighted. An efficient quadrature method of moments is used to approximate the general dynamics equation based on the particle size distributions, and the combustion model base on eddy dissipation concept (EDC) is employed to estimate the flame temperature field. The momentum, heat and mass transfer, Brownian coagulation and diffusion, surface growth, sintering and thermophoresis are taken into account. Excellent agreements between the predicted and experimental data, with respect to the flame temperature distribution and particle kinetics, are obtained.

For the final product of nanoparticles in the same flame field, the results show that the increasing of precursor loading leads to the larger agglomerated particles with larger size distribution. The self-preserving particle size distribution can be attained regardless of the variation of precursor loading, but the width of particle size distribution is slightly increased with increasing of inlet precursor loading. The primary particle number and size per agglomerate increase with the increasing of precursor loading, while the total SSA decreases. The variation of inlet precursor loading has a negligible effect of particle surface fractal dimension if only the variable of precursor loading is considered. As the inlet precursor loading is fixed, the increasing of carrying gas rate leads to the smaller agglomerated particles with increasing total SSA and width of particle size distribution, while the particles exhibit more irregular size and shape. The present study also proves that the particles with more irregular sizes and shapes have a better chance to coagulate and form the larger agglomerated particles.

Notation

a_a	surface area of agglomerated particles, m^2
a_p	surface area of the primary particle, m^2
a_{p0}	surface area of a monomer, m^2
A	total surface area per unit volume, m^2/m^3
$A_{\min}$	minimal total surface area per unit volume, m^2/m^3
C_c	Cunningham correction factor
d_a	mean agglomerated particle diameter, m
d_p	primary particle diameter, m
D_i	diffusion coefficient for species i, m^2/s
D_s	surface fractal dimension
E_A	activation energy, J/mol
G	the nucleus volume growth rate, m^3/s
H	flame height, mm
J	nucleation rate, m^3/s
k	the overall oxidation rate of $TiCl_4$, s^{-1}
k_b	Boltzmann constant, J/K
k_g	the constant of gas phase reaction rate, s^{-1}
k_0	pre-exponential term of the characteristic coalescence time, m^{-4}
k_s	the constant of surface reaction rate, m/s
m_k	kth moment of PSD
n_p	primary particle number per agglomerate
N	particle number, m^{-3}
N_{av}	Avogadro's number
NQ	order of the quadrature formulation
Q_m	methane flow rate, l/min
s	collision factor
SSA	specific surface area, m^2/g
T	gas temperature, °C
T_m	maximum flame temperature, °C
u	velocity of the flow field, m/s
u_{th}	the thermophoretic velocity, m/s
v, v'	particle volume, m^3
v^*	the volume of a TiO_2 monomer, m^3
v_i	ith eigenvector
w_i	weight of the quadrature approximation, m^{-3}
Y_i	local concentration of species i, mol/m^3

Greek letters

δ	Kronecker delta function
ρ_g	gas density, kg/m^3
ρ_p	particle density, kg/m^3
σ_g	geometric standard deviation
τ_f	characteristic coalescence time, s
Γ_B	particle Brownian diffusivity, m^2/s

Γ_t particle turbulent diffusivity, m^2/s
ω_i the monomer production rate by chemical reaction, $mol/m^3/s$

Acknowledgements

This work is supported financially by the research grant from the Key Project of the National Natural Science Foundation of China (Grant no. 10632070).

References

Akhtar, M.K., Xiong, Y., Pratsinis, S.E., 1991. Vapor synthesis of titania powder by titanium tetrachloride oxidation. A.I.Ch.E. Journal 37, 1561–1570.

Artelt, C., Schmid, H.J., Peukert, W., 2003. On the relevance of accounting for the evolution of the fractal dimension in aerosol process simulations. Journal of Aerosol Science 34, 511–534.

Briesen, H., Fuhrmann, A., Pratsinis, S.E., 1998. The effect of precursor in flame synthesis of SiO_2. Chemical Engineering Science 53 (20), 4105–4112.

Chan, T.L., Lin, J.Z., Zhou, K., Chan, C.K., 2006. Simultaneous numerical simulation of nano and fine particle coagulation and dispersion in a round jet. Journal of Aerosol Science 37, 1545–1561.

Formenti, M., Juillet, F., Meriaudeau, P., Teichner, S.J., Vergnon, P., 1972. Aerosols and Atmospheric Chemistry. Academic Press, New York, p. 79.

Friedlander, S.K., 2000. Smoke Dust and Haze: Fundamentals of Aerosol Behavior. Wiley, New York.

Gelbard, F., Seinfeld, J.H., 1980. Simulation of multicomponent aerosol dynamics. Journal of Colloid and Interface Science 78, 485–501.

Giesen, B., Orthner, H.R., Kowalik, A., Roth, P., 2004. On the interaction of coagulation and coalescence during gas-phase synthesis of Fe-nanoparticle agglomerates. Chemical Engineering Science 59, 2201–2211.

Hinds, W.C., 2000. Aerosol Technology: Properties, Behavior and Measurement of Airborne Particles. Wiley, New York.

Hulburt, H.M., Katz, S., 1964. Some problems in particle technology. Chemical Engineering Science 19, 555–574.

Johannessen, T., Pratsinis, S.E., Livbjerg, H., 2000. Computational fluid-particle dynamics for the flame synthesis of alumina particles. Chemical Engineering Science 55, 177–191.

Johannessen, T., Pratsinis, S.E., Livbjerg, H., 2001. Computational analysis of coagulation and coalescence in the flame synthesis of titania particles. Powder Technology 118, 242–250.

Koch, W., Friedlander, S.K., 1990. The effect of particle coalescence on the surface area of a coagulating aerosol. Journal of Colloid and Interface Science 140, 419–427.

Li, J., Matos, H.A., Azevedo, E.G., 2004. Two-phase homogeneous model for particle formation from gas-saturated solution processes. The Journal of Supercritical Fluids 32, 275–286.

Lin, J.Z., Chan, T.L., Liu, S., Zhou, K., Zhou, Y., Lee, S.C., 2007. Effects of coherent structures on nanoparticle coagulation and dispersion in a round jet. International Journal of Nonlinear Sciences and Numerical Simulation 8, 45–54.

Lu, S.Y., Lin, H.C., Lin, C.H., 1999. Modeling particle growth and deposition in a tubular CVD reactor. Journal of Crystal Growth 200, 527–542.

Magnussen, B.F., 1981. On the structure of turbulence and a generalized Eddy dissipation concept for chemical reaction in turbulent flow. In: Nineteenth AIAA Meeting, St. Louis.

Marchisio, D.L., Pikturna, J.T., Fox, R.O., Vigil, R.D., Barresi, A.A., 2003a. Quadrature method of moments for population-balance equations. A.I.Ch.E. Journal 49, 1266–1276.

Marchisio, D.L., Vigil, R.D., Fox, R.O., 2003b. Quadrature method of moments for aggregation–breakage processes. Journal of Colloid and Interface Science 258, 322–334.

McGraw, R., 1997. Description of aerosol dynamics by the quadrature method of moments. Aerosol Science and Technology 27, 255–265.

Miller, S.E., Garrick, S.C., 2004. Nanoparticle coagulation in a planar jet. Aerosol Science and Technology 38, 79–89.

Morgan, N.M., Wells, C.G., Goodson, M.J., Kraft, M., Wagner, W., 2006. A new numerical approach for the simulation of the growth of inorganic nanoparticles. Journal of Computational Physics 211, 638–658.

Pratsinis, S.E., 1988. Simultaneous nucleation, condensation, and coagulation in aerosol reactors. Journal of Colloid and Interface Science 124 (2), 416–427.

Pratsinis, S.E., 1998. Flame aerosol synthesis of ceramic powders. Progress in Energy and Combustion Science 24, 197–219.

Pratsinis, S.E., Vemury, S., 1996. Particle formation in gases: a review. Powder Technology 88, 267–273.

Pratsinis, S.E., Zhu, W., Vemury, S., 1996. The role of gas mixing in flame synthesis of titania powders. Powder Technology 86, 87–93.

Schwade, B., Roth, P., 2003. Simulation of nano-particle formation in a wall-heated aerosol reactor including coalescence. Journal of Aerosol Science 34, 339–357.

Settumba, N., Garrick, S.C., 2003. Direct numerical simulation of nanoparticle coagulation in a temporal mixing layer via moment method. Journal of Aerosol Science 34, 149–167.

Smagorinsky, J., 1963. General circulation experiments with the primitive equation. Monthly Weather Review 91, 99–164.

Spicer, P.T., Chaoul, O., Tsantilis, S., Pratsinis, S.E., 2002. Titania formation by $TiCl_4$ gas phase oxidation, surface growth and coagulation. Journal of Aerosol Science 33, 17–34.

Talukdar, S.S., Swihart, M.T., 2004. Aerosol dynamics modeling of silicon nanoparticle formation during silane pyrolysis: a comparison of three solution methods. Journal of Aerosol Science 35, 889–908.

Ulrich, G.D., 1971. Theory of particle formation and growth in oxide synthesis flames. Combustion Science and Technology 4, 47–57.

Ulrich, G.D., Riehl, J.W., 1982. Aggregation and growth of submicron oxide particles in flames. Journal of Colloid and Interface Science 87, 257–265.

Upadhyay, R.R., Ezekoye, O.A., 2003. Evaluation of the 1-point quadrature approximation in QMOM for combined aerosol growth laws. Journal of Aerosol Science 34, 1665–1683.

Wang, G., Garrick, S.C., 2005. Modeling and simulation of titania synthesis in two-dimensional methane–air flames. Journal of Nanoparticle Research 7, 621–632.

Wang, L., Vigil, R.D., Fox, R.O., 2005. CFD simulation of shear-induced aggregation and breakage in turbulent Taylor–Couette flow. Journal of Colloid and Interface Science 285, 167–178.

Wells, C.G., Kraft, M., 2005. Direct simulation and mass flow stochastic algorithms to solve a sintering-coagulation equation. Monte Carlo Methods and Applications 11 (2), 175–198.

Xiong, Y., Pratsinis, S.E., Weimer, A., 1992. Modeling and formation of boron carbide particles in an aerosol flow reactor. A.I.Ch.E. Journal 38, 1685–1692.

Xiong, Y., Pratsinis, S.E., 1993. Formation of agglomerate particles by coagulation and sintering—part 1: a two-dimensional solution of the population equation. Journal of Aerosol Science 24 (3), 283–300.

Yu, M.Z., Lin, J.Z., Chen, L.H., Chan, T.L., 2006. Large eddy simulation of a planar jet flow with nanoparticle coagulation. Acta Mechanica Sinaca 22, 293–300.

Yu, M.Z., Lin, J.Z., Chan, T., 2007. Numerical simulation of nanoparticle synthesis in diffusion flame reactor. Powder Technology 180, 9–20.